

PREPARATION OF A DUAL WAVELENGTH SEQUENCE OF HIGH-RESOLUTION SOLAR PHOTOSPHERIC IMAGES USING PHASE DIVERSITY

MATS G. LÖFDAHL,¹ THOMAS E. BERGER, RICHARD S. SHINE, AND ALAN M. TITLE
Lockheed Martin Missiles & Space Advanced Technology Center, 3251 Hanover Street, Palo Alto, CA 94304
Received 1997 April 8; accepted 1997 October 7

ABSTRACT

The collection, seeing compensation, and temporal filtering of a high-resolution time-sequence of solar photospheric images is described. A 70 minute time series of cospatial and cotemporal *G* band 4305 Å and wideband 4686 Å filtergrams was obtained with the 50 cm Swedish Vacuum Solar Telescope on the island of La Palma, Spain. The 29" × 70" field-of-view near disk center contains both an enhanced network region and an (apparently) nonmagnetic “quiet” region of granulation. The mean time between frames is 23.5 s. Each frame is created with partitioned phase-diverse speckle restoration of three realizations of the atmospheric turbulence acquired rapidly in sequence. The result is high-resolution movies of the solar photosphere, good enough to allow detection, tracking, and analysis of ~0.2 bright points. This analysis is the subject of a companion paper.

Subject headings: Sun: granulation — Sun: photosphere — techniques: image processing — techniques: interferometric

1. INTRODUCTION

Production of a data set suitable for studying the dynamics of solar magnetic elements on scales below 0.5 is an extremely difficult task in ground-based solar physics. The minimum requirements for observation of magnetic element dynamics are a very high spatial resolution ($\lesssim 0.3$; Title & Berger 1996) with a high degree of uniformity from frame to frame, a wide field of view (FOV $\sim 1'$), and continuous observations at a cadence on the order of 10 s for periods on the order of hours. This paper describes the observations and restoration techniques used to produce such a data set, which is analyzed in a companion paper (Berger et al. 1998, henceforth Paper II).

The detailed basis for these requirements is demonstrated in Paper II. Among the reasons are: the characteristic observed size of magnetic elements is about 250 km (0.35, Muller 1994). Observation of magnetic elements is frequently carried out indirectly through images of continuum, line center, and molecular band bright points. Berger et al. (1995) have demonstrated that magnetic elements are seen with particularly high contrast in filtergrams taken in the 4305 Å molecular bandhead of CH (the *G* band). Furthermore, Scharmer (1995, private communication) demonstrated that simultaneous images in *G*-band and continuum wavelengths can be combined to produce images that trace *G*-band bright points extremely well. This property is used in Paper II. Time series observations of *G*-band bright points show them to be highly dynamic objects. The characteristic time for fragmentation and merging is in the range of the granular evolution time (6–8 minutes) but significant morphological changes of individual elements can occur on timescales of 100 s. Large clusters from which smaller elements frequently fragment and recombine have observed lifetimes on the orders of hours in enhanced network regions.

Seeing is, of course, the primary obstacle to obtaining

high-resolution time series observations from the ground. Turbulence in the atmosphere above the telescope randomly distorts the phase of the wavefronts emanating from the Sun. The result is blurring and geometrical distortions in the collected images. Relative geometric distortions between frames can be successively removed by cross-correlative “destretching” techniques (Shine et al. 1994; Topka, Tarbell, & Title 1986; Tarbell, Title, & Schoolman 1979), but blurring is not corrected by these methods. Successful blur correction of solar images has been demonstrated with speckle interferometry (Keller & von der Lühe 1992; de Boer, Kneer, & Nesis 1992; de Boer & Kneer 1992; von der Lühe 1993; 1994); however, the amounts of data that needs to be collected makes it impractical for longer time sequences.

Recently developed methods, which estimate the wavefront over isoplanatic areas from multiphase, or “phase diverse,” images address this problem. The technique of phase diversity (PD) was first proposed by Gonsalves & Chidlaw (1979) as a method for simultaneously estimating the wavefront aberrations and the underlying object from two (or more) simultaneous images with a known phase difference (most commonly a difference in focus position). Paxman et al. (1992) suggested phase-diverse speckle (PDS), a joint estimation of the aberrations and the common object in a time sequence of phase-diverse data. The extra realizations fill in missing information at spatial frequencies where single optical transfer functions (OTFs) are zero. When processed jointly, the inversions also benefit from a more favorable ratio of data points to estimated parameters. Still, a small number of atmospheric realizations is sufficient for good restorations, significantly reducing the amount of data needed compared to speckle methods (Paxman et al. 1996). This eases the data storage requirements for a given sample rate and increases the chances of getting good enough data in each sample interval. Another appealing property of phase diversity methods is that they estimate and correct for the total wavefront of the optical system, including telescopic aberrations.

PD techniques are now used by several groups for making time sequences of fine-scale solar features. Löfdahl

¹ Large parts of this analysis were performed while M. G. L. was with the Royal Swedish Academy of Sciences, Stockholm Observatory, S-133 36 Saltsjöbaden, Sweden.

(1996) restored a 29" squared subfield of the 70 minute sequences discussed in this paper. Seldin et al. (1996) restored a 13.5 minute, 3".7 squared sequence of images from a plage region collected in 656 nm with the 76 cm Vacuum Tower Telescope at Sacramento Peak, New Mexico. Tritschler, Schmidt, & Knölker (1997) are in the process of restoring the 23" squared FOV of their 90 minutes of phase diverse sunspot images, observed in 569 nm with the 70 cm Vacuum Tower Telescope in Tenerife, Spain. The solar features in the latter two sequences have yet to be analyzed.

The implementation of PDS used here has been thoroughly tested and successfully applied to real data by Löfdahl & Scharmer (1994). Further verification of its correctness is provided by the joint effort of Paxman et al. (1996), who processed the same photospheric dataset with two different implementations of PDS, as well as with traditional speckle interferometry, producing essentially identical restored images.

The time sequences we describe in this paper consist of about 180 simultaneous *G*-band 4305 Å and 4686 Å wide-band filtergrams of an enhanced network region at disk center. The temporal cadence of the time series is roughly 25 s spanning a period of 71 minutes. Spatial resolution has been restored separately in the two wavelengths to near the diffraction limit ($\sim 0''.2$). The restored FOV is 29" \times 70".

Section 2 gives an overview of our PDS algorithm and introduces notation used in the following sections; § 3 describes the observations in more detail; § 4 describes the phase diversity image restoration; § 5 describes the assembly of the images to produce a temporal sequence (movie).

2. PARTITIONED PHASE DIVERSE SPECKLE

Here we give only a short (and slightly simplified) overview of our PDS implementation. A more complete description is given by Löfdahl & Scharmer (1994) and Paxman et al. (1996, § 3.2). With notation established in the latter paper, we now refer to our method as partitioned phase-diverse speckle (PPDS) since the wavefronts are determined from single atmospheric realizations, but the full PDS information is used for the estimation of the common object. A PDS data set consists of J phase-diverse image pairs where the object (the solar surface) can be assumed to be the same. Ideally, the only difference between these image pairs is that they sample different realizations of the atmospheric turbulence. The only difference between the images *in* a pair is a known phase, most commonly a change in focus.

The phase, ϕ_j , of a wavefront is expanded in a linearly independent set of basis functions,

$$\phi_j(u) = \sum_{m=4}^M \alpha_{jm} \psi_m(u), \quad (1)$$

where u is a two-dimensional coordinate on the aperture. Here ψ_m are Zernike polynomials as defined by Noll (1975). The expansion starts with the focus term, $m = 4$, and is truncated at some number M . The wavefront estimation consists of determining the coefficients, α_{jm} , by minimizing an error metric that measures the consistency between the observed images and the estimated object and wavefront in a least-squares sense. Our code uses an iterative linearization technique to find the optimum estimates of the wavefronts.

In the Fourier domain, the error metric for atmospheric

realization j can be written as

$$L_j = \sum_u \sum_k \gamma_k |H_j D_{jk} - \hat{F}_j \hat{S}_{jk}|^2, \quad (2)$$

where D_{jk} is an image collected in diversity channel k and \hat{S}_{jk} is an estimate of the corresponding optical transfer function (OTF). The OTFs are the autocorrelations of the corresponding generalized pupil functions, taking both $\phi_j(u)$ and the known focus difference into account. \hat{F}_j is the single realization estimate of the object and H_j is a noise filter that minimizes the rms difference between \hat{F}_j as calculated with filtered noisy data and noiseless unfiltered data. The noise variance ratio, γ_k , is given by

$$\gamma_k = \sigma_1^2 / \sigma_k^2, \quad (3)$$

where σ_k is the rms noise of diversity channel k .

In a second step, the optimum estimate of the object, common to the PDS data set, is formed according to the formula

$$\hat{F} = H \frac{\sum_{j=1}^J \sum_k \gamma_k D_{jk} \hat{S}_{jk}^*}{\sum_{j=1}^J \sum_k \gamma_k |\hat{S}_{jk}|^2}, \quad (4)$$

where H is similar to H_j , but takes data from all J realizations into account,

$$H = 1 - \langle |N_1|^2 \rangle \left\langle \frac{\sum_{j=1}^J \sum_k \gamma_k |\hat{S}_{jk}|^2}{|\sum_{j=1}^J \sum_k \gamma_k D_{jk} \hat{S}_{jk}^*|^2} \right\rangle, \quad (5)$$

where $\langle |N_1|^2 \rangle$ is the noise power in diversity channel 1 and the angle brackets denote an expectation value, see (Löfdahl & Scharmer 1994) for details. One example of an H filter is shown in Figure 7 below.

3. OBSERVATIONS

Phase-diverse data were collected with the 50 cm Swedish Vacuum Solar Telescope (SVST,² Scharmer et al. 1985) on La Palma on 1995 October 5 between 10:57 and 12:08 UT.

3.1. Tracking

Telescope pointing and jitter correction were accomplished in real-time using a newly developed granulation correlation tracking system. The system uses a Dalsa CA-D1-0128 CCD camera with a wideband 4920 Å filter to acquire granulation images over a 30" FOV; the image scale is 0''.4–0''.5 per pixel. The images are read at 820 frames per second through a DMA interface to a DEC Alpha 3000/900 275 MHz workstation. Every other image is cross-correlated over a user-selectable 32 \times 32 pixel subarea (approximately 20" \times 20") to a reference image of the tracked granulation which is updated every 30 s. The cross-correlation offsets are translated to commands that are sent at a 410 Hz rate to the damped (~ 20 Hz) servo-control of the M3 mirror. The system gives stable subarcsecond pointing during good ($\lesssim 0''.5$) seeing.

3.2. Data Collection

An area of both quiet Sun and enhanced network activity (exhibiting many *G*-band bright points) near disk center was observed using two Kodak Megaplug 1.6 1536 \times 1032 pixel 10 bit CCD cameras. Figure 1 shows the optical

² The aperture is stopped down to 47.5 cm by an external heat shield.

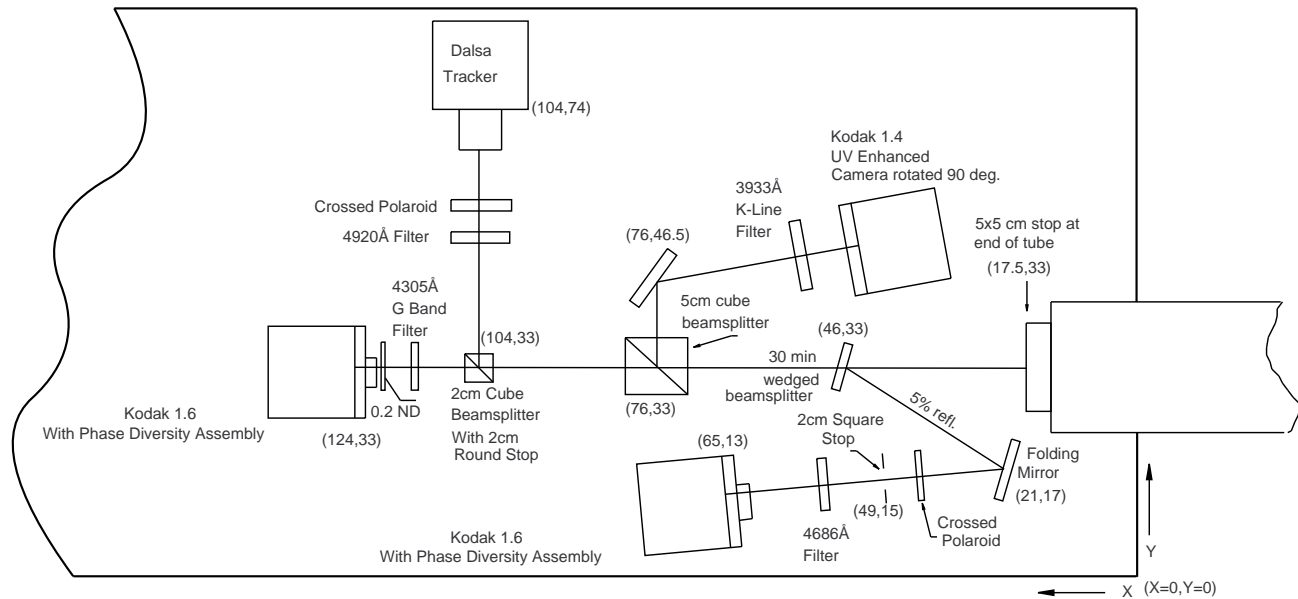


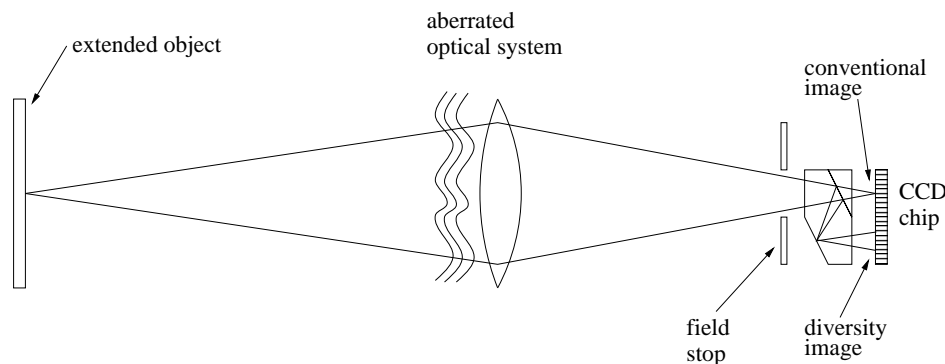
FIG. 1.—Optical setup used for multi-wavelength phase diversity observations: 1995 September–1995 October at the Swedish Vacuum Solar Telescope, La Palma. Coordinates are in cm. Ca II K line data were collected but without phase diversity; they are not discussed in this paper (courtesy of Darrel Torgerson).

arrangement. One camera used a 12 Å bandpass G-band interference filter (center wavelength 4305 Å) and the other used a 54 Å bandpass interference filter (center wavelength 4686 Å). The image scale is 0".083 pixel⁻¹; the diffraction limited (λ/D) resolution is 0".187 (12% oversampling) in the G band and 0".203 (22% oversampling) in the 4686 Å wideband. The shutters of the two cameras were synchronized by computer control and the integration time was 20 ms. Both cameras were equipped with phase-diverse beam splitters (see Fig. 2) which put two images on each CCD with a difference in focus position corresponding to 8.85 mm (± 0.1 mm) in air. This is equivalent to 1.16 and 1.06 waves peak-to-peak of defocus in the G band and in the wideband, respectively.

Frame selection was carried out on the G-band camera; the best three frames from each 20 s evaluation period, and the simultaneous wideband frames, were recorded for later processing. Intervals of 20 s are used in order to sample over

a wide range of seeing conditions while also insuring that minimal solar evolution occurs between the selected images from adjacent intervals. With overhead for writing the images to disk, the average cadence of the selection intervals is 23.5 s. The frames that are selected are usually recorded within seconds of each other since good seeing tends to occur intermittently. This justifies the assumption of a common object for the three image pairs ($J = 3$).

The cameras use separate mechanical focal plane shutters triggered by a synchronized pulse from the control computer. However, the direction of shutter motion is not under control of the observer; a synchronization error on the order of the focal plane traversal time of 8.4 ms could result from opposite shutter motion. Within each separate camera, the finite shutter traversal time also results in a time delay between the two phase diversity exposures of about 4.2 ms. These delay times are not negligible with respect to either atmospheric seeing evolution or the nominal integra-



Phase diversity optical setup -schematic
Puts focused-defocused images on one CCD chip

FIG. 2.—The beam-splitter configuration was designed by Göran Scharmer and manufactured by Interoptics. The beam-splitter angle and the thickness of the glass give two degrees of freedom, enough to specify both the amount of diversity and the image separation on the CCD (courtesy of Göran Scharmer).

tion time of 20 ms; we show below that this delay is a probable source of error in the reconstruction process.

Dark frames were collected at the end of the day by blocking the beam from the telescope. No flat fields were recorded this day, but the day before flat fields were collected by moving the table 200 cm out of focus and rapidly scanning an area of quiet Sun by oscillating the M3 mirror.

4. WAVEFRONT SENSING AND IMAGE RESTORATION

4.1. *The Phase Diverse Speckle Data Set*

The *G*-band and wideband image sequences were aligned with cross-correlations of the focused images to compensate for camera misalignments. The $29'' \times 70''$ region chosen for restoration and analysis encompasses most of the usable FOV of the phase-diversity beam splitters. In addition, the diversity channels (with different focus positions) were brought into approximate registration by cross-correlating a small number of focused images with their corresponding defocused images. The procedure to achieve subpixel accuracy of this alignment is described in the next section.

The processing was applied to 70×70 pixel ($5''.8 \times 5''.8$) subfields. The subfield size is a tradeoff, in that large subfields contain more information that can facilitate the inversions but small subfields avoid averaging out anisoplanatic wavefront variations. Previous experience with data from the SVST indicates that isoplanatic image formation is a reasonable approximation in subfields on the order of $5''$ squared. Successful inversions of such data have been performed by Löfdahl & Scharmer (1994) and Paxman et al. (1996). To avoid edge effects, FFTs were performed on larger (128×128 pixel) apodized arrays centered on the 70×70 pixel subfield.

4.2. *Parameter Setting and Preliminary Inversions*

During an experimental phase, the data were examined in different ways and a number of trial inversions were executed. The results of these experiments guided the setting of a number of parameters for the main inversions.

Illumination in the two channels is slightly different (due to the beam splitter) resulting in a noise variance ratio of $\gamma_2 = 0.3$ in the *G* band and $\gamma_2 = 0.4$ in the wideband. In the preliminary inversions we found that using these values improved the convergence slightly as compared to setting $\gamma_2 = 1$ ($\gamma_1 = 1$ by definition).

There are tradeoffs to consider when the order of expansion, M , is chosen, and the optimum choice can differ depending on the application. A high-order expansion allows a more detailed modeling of the wavefront, but if the quality of the data is bad, the solutions may become unphysical and/or entrapped in local minima.

In our code, the number of effectively free wavefront parameters can be adopted to the data quality automatically and independently of M by use of a cutoff in the singular value decomposition (SVD; see Press et al. 1992) method used to solve the linearized equations. We express the cutoff, w_c , as a fraction of the largest singular value. In our experience, choosing a high value for w_c allows physical solutions for many wavefront parameters, as evidenced by consistency with Kolmogoroff statistics. Using a high w_c for safety with bad data, a large M can be chosen to allow detailed modeling of good data. However, there is also the practical consideration that the computing-time scales linearly with the number of included wavefront parameters.

Therefore M should be chosen just large enough to give as much freedom as is practically useful with the good data.

In the main inversions, the wavefront expansion was truncated at $M = 21$. In a small number of test cases, $M = 15$ did not give restorations as good, while $M = 28$ did not improve the restored images significantly.

Preliminary inversions showed signs of entrapment in local minima with $w_c = 0.02$, which is the cutoff used for previous data with good results. The reason is probably the time delay between the diversity channels introduced by the lateral shutter motion. With the current data, we therefore used $w_c = 0.08$, which solved the entrapment problem.

A selected subset of good quality frames was pre-processed with the phase-diversity program, estimating subpixel interchannel registration. Using only good quality data for this step lets the worse data benefit from the parameters estimated from the better data. The registration parameters, averaged over the subfields and fitted to linear functions of observation time, were then kept fixed during the individual main inversions. In order to avoid having coma-type aberrations being interpreted as registration parameters, a high-order expansion, $M = 45$, of the wavefronts was used in this step. This reduced the variation of the estimated registration parameters significantly as compared to $M = 21$.

4.3. *Results of the Main Inversions*

The full data set consists of phase diverse data from 542 atmospheric realizations in two different wavelengths. With 60 (5×12) subfields per frame, the total number of wavefront determinations is 65,040. The average number of iterations required to converge wavefront corrections to less than 0.01 rad was 6.8 in the *G* band and 6.3 in the wideband. A total of 181 $29'' \times 70''$ (350×840 pixel) images were formed by combining restored subfields. In three selection intervals, all the atmospheric realizations are so bad that the object estimates are useless. These are excluded from the following analysis and from the restored image sequences. The total number of restored frames is therefore only 178.

The restoration algorithm ran on several DEC Alpha 9000 workstations in parallel over the course of several weeks; an estimated 2000 hr of processor time was required to produce this data set.

4.3.1. *Wavefronts*

Seeing is a random process, so one can expect the aberration coefficients α_m to vary a fair amount with time. However, the trends should be consistent with expected telescope aberrations. The estimated wavefronts agree well with the type of temporal evolution of the SVST aberrations estimated from 1993 data by Löfdahl & Scharmer (1994, Fig. 4). This evolution is attributed to heating of the entrance window and rotation of the optical elements of the alt-az telescope with respect to the image plane.

The individual wavefront coefficients estimated in the two wavelengths, α_m^{4686} and α_m^{4305} , correlate well but not perfectly. The linear correlation coefficient is 0.95 for the focus parameter ($m = 4$), and greater than 0.5 for most of the other parameters. Our conjecture is that a significant reason for the spread is seeing evolution during the timing errors due to the shutter motion (see § 3).

There are also systematic discrepancies that we illustrate in Figure 3, where $\langle \alpha_m^{4686} \rangle$ is scatter-plotted against $\langle \alpha_m^{4305} \rangle$. Linear fits, $\alpha_m^{4686} = c_m^0 + c_m^1 \alpha_m^{4305}$, show that $c_m^1 < 1$

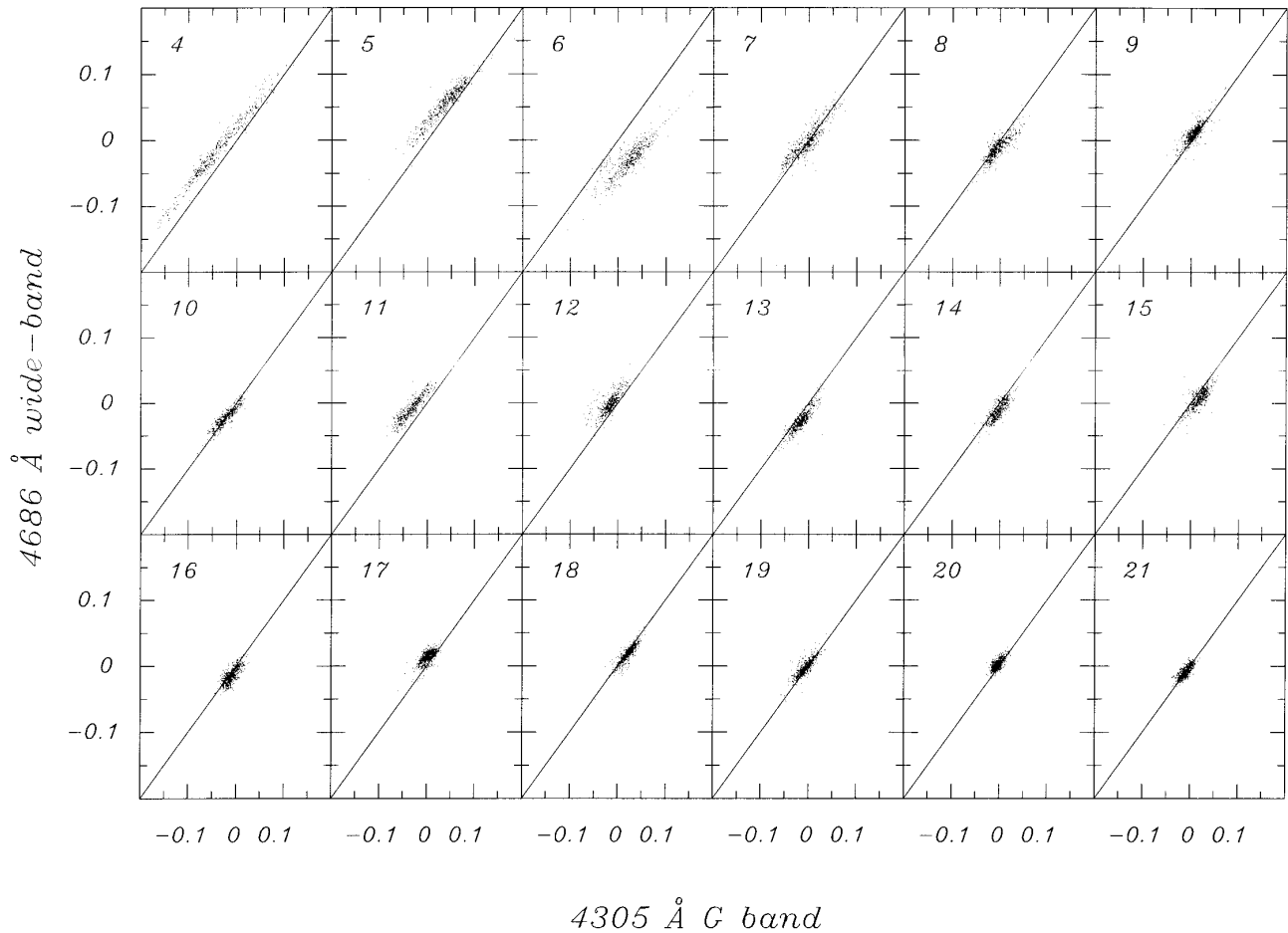


FIG. 3.—Scatter plots of wideband vs. G -band subfield-averaged Zernike coefficients, $\langle \alpha_m^{4686} \rangle$ and $\langle \alpha_m^{4305} \rangle$. The Zernike indices, m , are shown in the upper left corner of each tile. The low order indices correspond to focus ($m = 4$), astigmatism (5, 6), coma (7, 8, 9, 10), and spherical (11). The systematic deviations from the $y = x$ lines are consistent with differences in wavelength (and therefore also in contrast), passband, and two different optical paths.

for all m . Normalizing the wavefronts to the same wavelengths should correct this, but the systematic effect prevails, although with a smaller magnitude. Like the interchannel registration parameters, the differential aberrations between the two cameras appear to evolve slowly with time. Removing linear trends from the coefficients further increase the c_m^1 coefficients and improves the correlation coefficients slightly for almost all m . It also removes the constant offsets c_m^0 , particularly prominent in the focus, astigmatism, and spherical aberration terms. These offsets are consistent with the fact that the two wavelength channels were observed with two separate cameras (focus), separated at a wedged beam splitter (astigmatism) and passing through different amounts of glass (spherical).

It is somewhat puzzling that c_m^1 is still systematically less than 1 but inspection of the differences plotted as functions of time, shows that in many cases more complicated evolution takes place, which could be corrected by the removal of higher order fits. Such evolution could be caused by imperfect alignment of the optics after the beam splitter that separates the two wavelength channels. Another possible explanation is the difference in the objects in the two wavelengths. If the higher contrast in the G -band images make the PD wavefront sensing easier, that might allow the determination of additional effective parameters, as controlled by the SVD cutoff. This explanation is supported by c_m^1 values closer to unity as well as slightly higher correlation

coefficients for most wavefront parameters in the quiet granulation half of the FOV as compared to the half where most of the pointlike bright points are found. Another possible explanation is the fact that the wideband filter bandpass is ~ 4 times that of the G -band filter, and so would cause a slight averaging effect of the estimated wavefronts.

4.3.2. Restored Images

When all wavefronts are estimated, PPDS estimates of the object in each subfield are formed according to equation (4). The restored subfields are mosaicked so that reconstructions of the entire FOV are obtained. The improvement in a typical case is shown in Figure 4 (Plate 23). Slightly overlapping window functions, that taper off to zero about 10 pixels outside the 70×70 pixel FOVs, are used. This avoids artifacts from subfield mismatch. It should be noted that visual examination of earlier single restorations show very little of such effects (Löfdahl & Scharmer 1994), but this step is included because we wanted to avoid problems in the following subfield cross-correlation step (for destretching) and to ensure success without manual interaction with the large data set at hand.

For some cases, when the restored object mosaic quality was below average, various attempts were made to subjectively improve the quality. When the assumption of a common object was violated because the data were col-

lected too far apart in time, new restored images were formed using only two realizations ($J = 2$). The same action was taken in a few cases where the seeing in one of the realizations was much worse than in the other two. The final selection interval had only two realizations to start with, because of lost tracking. In some cases, new estimates of the wavefronts were made, but started from the subfield-averaged original wavefront instead of from zero.³ This sometimes helps individual subfields where the original inversion is trapped in a local optimum. In one case, severe ringing was observed, which was taken care of by using a slightly narrower noise filter, H , in the object formation. In total, about 10 object estimates (per wavelength sequence) were improved in one or more of these ways.

5. TIME-SEQUENCE PRODUCTION

5.1. Destretching

Following phase diversity restoration, the images were further processed to remove image rotation⁴ and relative atmospheric distortion between frames. The relative distortions are removed by “temporal destretching” as described in Shine et al. (1994). This method assumes that high-frequency distortions are atmospheric in origin and attenuates them. Lower frequency motions due to real surface flows are preserved. However, any high-frequency solar motions are also attenuated. This data set has a roughly normal distribution of time between frames with a minimum of 7 s, a maximum⁵ of 99 s, a mean of 23.7 s, and a standard deviation of 9.1 s. We define it as the “prefiltered” data set (see also § 5.2).

Examples of such images are shown in Figures 5 and 6 (Plates 24 and 25). The right portion of the FOV consists of relatively nonmagnetic granulation, while the left portion contains the enhanced network region. The white squares demarcate subregions which are analyzed individually in Paper II for magnetic field concentration effects.

5.2. Spacetime Filtering

The prefiltered data set is then phase velocity (or “spacetime”) filtered to suppress the solar acoustic p -mode waves and some of the remaining seeing noise as described in Title et al. (1992). Phase velocities above 4 km s^{-1} are attenuated with a sharp low-pass filter in the Fourier domain. The resulting reduction in p -mode intensity variations and random noise improves the frame-to-frame continuity of the movies considerably, thereby facilitating more accurate local correlation tracking. Filtering in the Fourier domain introduces an implicit interpolation in the temporal domain resulting in this case in a final uniform frame time of 23.75 s. We define this as the “filtered” data set.

5.3. Image Quality

The resolution in a restored image is limited by the passband of the filter, H (see equations [4] and [5]). Bad seeing attenuates the information at high spatial frequencies, so that it is hidden in noise. When this happens in all J frames in a PDS data set, the passband of H becomes narrower and

³ Only the original wavefronts are discussed in § 4.3.1.

⁴ The alz-az mounting of the SVST results in image rotation which amounted to a total of about 6° over the course of the observations analyzed here.

⁵ There are ~ 1 minute gaps in the sequences due to the removal of bad-quality frames and a pause in observations because of computer storage changes.



FIG. 7.—One example of the Fourier domain filter, H . Superimposed is a black ring with equivalent radius, U_H , see eq. (6). The radius of the black disk is the diffraction limit cutoff frequency.

the restored resolution suffers. We quantify the resolution in a frame by calculating an equivalent circular filter radius,

$$U_H = \sqrt{\frac{\sum_u H(u)}{\sum_u A(u)}}, \quad (6)$$

where $A(u)$ is a binary function that is unity inside the diffraction limit passband and zero outside (see Figure 7). The correspondence between resolution and seeing is shown in Figure 8 by comparison of U_H and the rms of the estimated wavefronts. Most of the time the seeing is quite even at

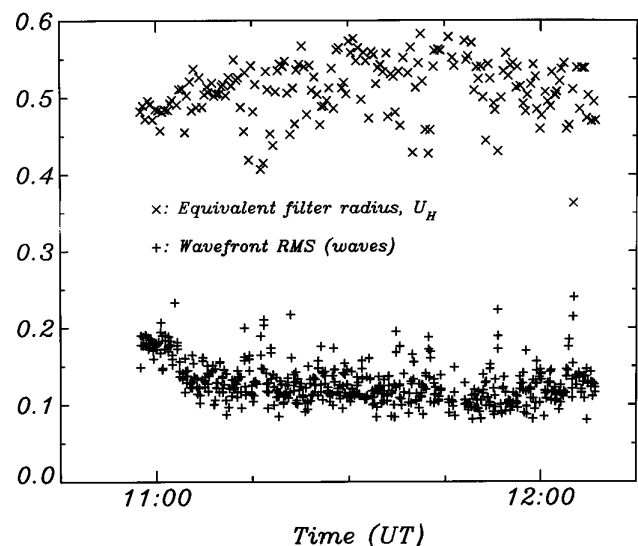


FIG. 8.—Evolution of resolution and wavefront rms in the G band. Crosses: U_H , equivalent radius of the H filter in units of the diffraction limit cutoff frequency, see eq. (6) (178 data points). Plus signs: rms of the estimated wideband wavefronts in waves, calculated as $(\sum_m \langle \sigma_m^{4.305} \rangle)^{1/2}$ where $\langle \cdot \rangle$ denotes averaging over subfields (533 points).

about 1/10 waves rms, although there are several examples of much worse seeing. All cases where $U_H \lesssim 0.45$ correspond to high-wavefront rms, while the widest filters ($U_H \approx 0.6$) correspond to moments with low-wavefront rms.

A circular filter with radius U_H would transmit spatial waves with a period of $\sim 0''.2/U_H$, so the $0.4 \lesssim U_H \lesssim 0.6$ range shown in Figure 8 corresponds to resolution in the range $\sim 0''.5-0''.3$. Bright points with FWHM equal to $\sim 0''.2$ are resolved in the $\sim 0''.4$ images, while most of the bright points are *not* resolved in the worst frames of our sequences. This is consistent with the findings of Title & Berger (1996), which show that observation of bright points in intergranular lanes requires spatial resolution on the order of $\sim 0''.3$ or better. Note that the resolutions are in fact slightly better than indicated in Figure 8, as the definition of U_H slightly underestimates the passband because H does not have a sharp edge.

In Figure 9 we show the contrast, a commonly used measure of image quality, of the observed focused images

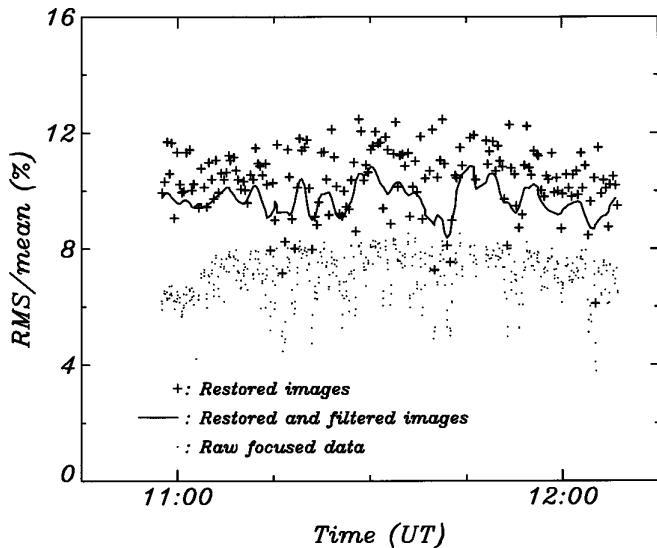


FIG. 9a

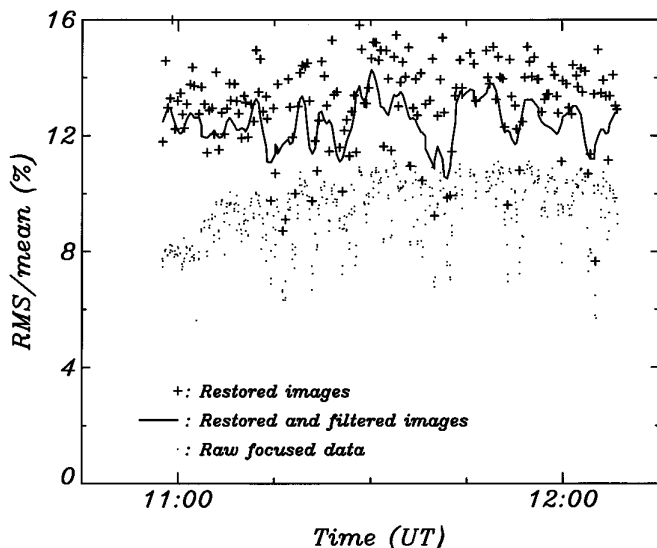


FIG. 9b

FIG. 9.—Temporal evolution of image rms contrast in the wideband (a) and G band (b). See Table 1 for statistics.

TABLE 1
RMS CONTRAST STATISTICS FOR RAW FOCUSED DATA,
PREFILTERED DATA SETS, AND FILTERED DATA SETS

Data Type	Maximum	Mean	Minimum	Sigma
Wideband 4686 Å:				
Raw data	8.5	7.1	3.8	0.8
Prefiltered	12.5	10.4	6.1	1.1
Filtered	10.9	9.7	8.4	0.5
G band 4305 Å:				
Raw data	11.1	9.4	5.6	1.1
Prefiltered	16.3	13.1	7.7	1.5
Filtered	14.2	12.5	10.5	0.7

and the restored frames as functions of time. There is a good correlation between the contrast of the observed images and the rms of the estimated wavefronts, e.g., the contrast is low when the rms of the wavefront is high. However, the restored image contrast is *very* low when all three observed images are blurry, the wavefront rms is high and U_H is relatively small. As can be seen in Table 1, the PDS processing increases the contrast, but it also amplifies the variation in contrast from frame to frame.⁶ The spacetime filtering lowers the average contrast a bit, but it significantly improves the stability.

6. CONCLUSIONS

Phase-diversity image restoration of solar photospheric images can produce the quality of time series data necessary for measuring subgranular scale flowfields in the photosphere (see Paper II). In addition, the frame-to-frame stability exhibited in the restored data is clearly superior to the unrestored data set; cross-wavelength alignment and destretching are improved significantly.

However, there are improvements which can be made in our implementation of the technique. For instance, the main reasons for the nonsystematic differences between the derived wavefronts in the G band and the wideband are (1) the use of two separate mechanical shutters for the OCDs, and (2) the large bandpass differences between the filters.

The evidence for (1) is the spread in the correlation of α_m^{4686} and α_m^{4305} (see § 3), the fact that we still require a destretching of wideband images onto the G-band images in order to properly map the bright points, and perhaps also in the relatively low correlation between some of the flowfield vectors measured from the restored G-band and wideband image sets (Paper II, § 4.2). Finally, we had to restrict the wavefront solutions (high w_c) much more than with previous similar data sets. We believe this is due to the 4.2 ms delay between the focused and the defocused images, as the shutter moves in front of the sensor array. The evidence for (2) is the systematically higher amplitudes of the G-band coefficients (see § 3), although this could also be caused by the higher contrast in the G band.

An obvious improvement would be to use a single shutter for the two beams. Using a wavelength for the wideband image which is closer to that of the G band, as well as a cube beam splitter located much closer to the cameras, would ensure that the two wavefronts would be practically the same (except for possible relative focus errors). This would

⁶ In very good seeing one would expect the PDS processing to restore all images to the same contrast, but when the seeing varies, better images have more information to facilitate the inversions.

decrease the magnitude of any wavefront error between the wavelengths and improve the calculation of the difference between the G -band and the wideband intensities. The use of a single shutter would also allow both the wideband and the G -band images to be used for the wavefront determinations through a straight-forward extension of the error metric (see eq. [2]),

$$L_j = \sum_{\lambda} \sum_k \sum_u |H_{j\lambda} D_{jk\lambda} - \hat{F}_{j\lambda} \hat{S}_{jk\lambda}|^2 / \sigma_{k\lambda}^2, \quad (7)$$

where the λ index refers to two (or more) wavelength channels. The objects, $\hat{F}_{j\lambda}$, and the observed images, $D_{jk\lambda}$, are unrelated in different wavelengths, but the transfer functions, $\hat{S}_{jk\lambda}$, only differ by the known fixed focus difference and slowly evolving aberration differences which could be estimated in preprocessing along with the interchannel registration in PPDS (and together with all other parameters in joint phase-diverse speckle [JPDS]). Because of the difference in wavelength between the cameras, the natural

choice of units for the Zernike coefficients is then not waves or radians anymore, but length.

This work was supported by NASA contracts NAS 5-30386 at Stanford and NAS 8-39747 and Independent Research Funds at Lockheed-Martin. While in Sweden, M. G. L. was supported by the Swedish Science Research Council. Göran Scharmer provided Figure 2, as well as helpful comments and suggestions. Darrel Torgerson performed the optical layout at SVST and also produced Figure 1. The SVST is operated by the Swedish Royal Academy of Sciences at the Spanish Observatorio del Roque de los Muchachos of the Instituto de Astrofísica de Canarias (IAC). Paco Armas, Göran Hosinsky, Rolf Kever, and Wang Wei maintain the SVST in its status as one of the premiere solar telescopes in the world. The staff of the IAC are thanked for providing excellent accommodations and assistance at La Palma.

REFERENCES

- Berger, T. E., Löfdahl, M. G., Title, A. M., & Shine, R. S. 1998, *ApJ*, 495, 973 (Paper II)
- Berger, T. E., Schrijver, C. J., Shine, R. S., Tarbell, T. D., Title, A. M., & Scharmer, G. 1995, *ApJ*, 454, 531
- de Boer, C. R., & Kneer, F. 1992, *A&A*, 264, L24
- de Boer, C. R., Kneer, F., & Nesis, A. 1992, *A&A*, 257, L4
- Gonsalves, R. A., & Chidlaw, R. 1979, *Proc. SPIE*, 207, 32
- Keller, C. U., & von der Lühe, O. 1992, *A&A*, 261, 321
- Löfdahl, M. G. 1996, Ph.D. thesis, Stockholm Univ.
- Löfdahl, M. G., & Scharmer, G. B. 1994, *A&AS*, 107, 243
- Muller, R. 1994, in *Solar Surface Magnetism*, ed. R. J. Rutten & C. J. Schrijver (Dordrecht: Kluwer), 73
- Noll, R. J. 1975, *J. Op. Soc. Am.*, 66, 207
- Paxman, R. G., Schulz, T. J., & Fienup, J. R. 1992, *J. Op. Soc. Am. A*, 9, 1072
- Paxman, R. G., Seldin, J. H., Löfdahl, M. G., Scharmer, G. B., & Keller, C. U. 1996, *ApJ*, 466, 1087
- Press, W. H., Teukolsky, S. A., Vetterling, W. T., & Flannery, B. P. 1992, *Numerical Recipes in C, The Art of Scientific Computing*, 2nd ed. (Cambridge: Cambridge Univ. Press)
- Scharmer, G. B., Brown, D. S., Peterson, L., & Reben, J. 1985, *Appl. Opt.*, 24, 2558
- Seldin, J. H., Paxman, R. G., & Keller, C. U. 1996, *Proc. SPIE*, 2804, 166
- Shine, R. A., Title, A. M., Tarbell, T. D., Smith, K., Frank, Z. A., & Scharmer, G. 1994, *ApJ*, 430, 413
- Tarbell, T. D., Title, A. M., & Schoolman, S. A. 1979, *ApJ*, 229, 387
- Title, A. M., & Berger, T. E. 1996, *ApJ*, 463, 797
- Title, A. M., Topka, K. P., Tarbell, T. D., Schmidt, W., Balke, C., & Scharmer, G. 1992, *ApJ*, 393, 782
- Topka, K. P., Tarbell, T. D., & Title, A. M. 1986, *ApJ*, 306, 304
- Tritschler, A., Schmidt, W., & Knolker, M. 1997, in *ASP Conf. Ser. 118, Advances in the Physics of Sunspots*, ed. B. Schmieder, J. C. del Toro Iniesta, & M. Vasquez (San Francisco: ASP), 170
- von der Lühe, O. 1993, *A&A*, 268, 374
- . 1994, *A&A*, 281, 889